Journal of Hydrology 632 (2024) 130876

Contents lists available at ScienceDirect

Journal of Hydrology

journal homepage: www.elsevier.com/locate/jhydrol

Research papers

Fusing daily snow water equivalent from 1980 to 2020 in China using a spatiotemporal XGBoost model

Liyang Sun [a], Xueliang Zhang [a,b,*], Pengfeng Xiao [a,b,c], Huadong Wang [a], Yunhan Wang [a], Zhaojun Zheng [d]

[a] Jiangsu Provincial Key Laboratory of Geographic Information Science and Technology, Key Laboratory for Land Satellite Remote Sensing Applications of Ministry of Natural Resources, School of Geography and Ocean Science, Nanjing University, Nanjing, Jiangsu 210023, China

[b] Frontiers Science Center for Critical Earth Material Cycling, Nanjing University, Nanjing, Jiangsu 210023, China

[c] Jiangsu Center for Collaborative Innovation in Geographical Information Resource Development and Application, Nanjing, Jiangsu 210023, China

[d] The National Satellite Meteorological Center, Beijing 100081, China

ARTICLE INFO

This manuscript was handled by Marco Borga, Editor-in-Chief, with the assistance of Francesco Avanzi, Associate Editor

Keywords:
Snow water equivalent
Extreme gradient boosting
Data fusion
Machine learning

ABSTRACT

Accurate snow water equivalent (SWE) data are crucial for estimating the water supply capacity of snow and are of profound importance for the communities of hydrology, climatology, and ecology. However, existing SWE products suffer from varying degrees of uncertainty, incompleteness, and inconsistency. This study proposes a novel spatiotemporal fusion model to estimate SWE by combining multisource SWE products (GlobSnow, ERA-Interim, ERA5-Land, GLDAS, and CSWE) and spatiotemporal covariates (land cover, temperature, snow-related, geospatial, and temporal features) with the extreme gradient boosting (XGBoost) model. Specifically, the proposed spatiotemporal XGBoost model can encapsulate the advantages of multisource SWE products and address the nonlinear relations between SWE and its influencing variables. Furthermore, it embeds the geospatial and temporal features to capture the heterogeneities of SWE. Evaluation results on daily SWE records from 647 meteorological sites in China show that the proposed XGBoost SWE outperforms existing SWE products and other fusion methods (RF, SVM, RR, SA, and MLR), which demonstrates the effectiveness of the model with R values of 0.77, 0.70 and MAE and RMSE values of 7.54, 8.62 mm and 12.29, 13.73 mm based on cross-validation according to year and site, respectively. Using the proposed model, a dataset of daily SWE from 1980 to 2020 with a spatial resolution of 25 km over China is provided, aiming to deliver accurate SWE data for hydrological research and water resource management.

1. Introduction

Snow occupies over 50 % of the land area in the Northern Hemisphere during the winter and is a crucial element of the cryosphere and global energy cycle due to its high albedo and low thermal conductivity (Barnett et al., 1988; Flanner et al., 2011; Frei and Robinson, 1999). Snowmelt runoff provides a stable and reliable water supply for terrestrial rivers in mid- and high-latitude areas, and more than one-sixth of the world population depends upon glaciers and seasonal snowpacks for water (Barnett et al., 2005; Griessinger et al., 2016). Snow Water Equivalent (SWE) is a measure of the water content in a snowpack and represents the amount of water available for runoff. Therefore, it has significant impacts on hydrological processes, climate, and ecosystems (Bintanja and Andry, 2017).

SWE estimation methods include spatial interpolation estimation based on ground-measured sites (Dozier et al., 2016), data assimilation (Takala et al., 2011), passive microwave remote sensing inversion (Jiang et al., 2022), active microwave remote sensing inversion (Painter et al., 2016), reconstruction (Molotch and Margulis, 2008; Premier et al., 2023; Rittger et al., 2016), physical models (Brun et al., 2013; Fontrodona-Bach et al., 2023), and lidar measurement technology (Deems et al., 2013). Among the various methods, passive microwave remote sensing inversion, data assimilation, and reconstruction methods are widely used to produce vast-area and long-term SWE products, namely, satellite-based SWE, data assimilation SWE, and reanalysis SWE, respectively.

* Corresponding author at: Jiangsu Provincial Key Laboratory of Geographic Information Science and Technology, Key Laboratory for Land Satellite Remote Sensing Applications of Ministry of Natural Resources, School of Geography and Ocean Science, Nanjing University, Nanjing, Jiangsu 210023, China.
E-mail address: zxl@nju.edu.cn (X. Zhang).

https://doi.org/10.1016/j.jhydrol.2024.130876
Received 2 July 2023; Received in revised form 10 January 2024; Accepted 25 January 2024
Available online 16 February 2024

Satellite-based SWE products observe brightness temperature as a function of snowpack properties and possess advantages in identifying the spatial pattern and temporal variation of SWE, mainly including the Advanced Microwave Scanning Radiometer for the Earth Observing System (AMSR-E) SWE (Kelly, 2009), AMSR2 SWE (Imaoka et al., 2010; Tedesco and Jeyaratnam, 2019), and China's SWE Remote Sensing Dataset from 1980 to 2020 (CSWE) (Jiang et al., 2022). Data assimilation SWE products are generally derived from Land Data Assimilation Systems by using ground-based observations, remote sensing products, and/or reanalysis forcing, such as the Global Snow Monitoring for Climate Research (GlobSnow) SWE (Luojus et al., 2021) and the Global Land Data Assimilation System (GLDAS) (Rodell et al., 2004). Compared to data assimilation SWE, reanalysis SWE products provide relatively more continuous and integral records based on a numerical weather prediction model, which assimilates earth observations over a long historical period into the weather prediction model. The reanalysis SWE products mainly include the fifth generation of the European Centre for Medium-Range Weather Forecasts (ECMWF) atmospheric reanalysis of the global climate (ERA5-Land) SWE (Muñoz-Sabater et al., 2021), Interim version of ECMWF atmospheric reanalysis of the global climate (ERA-Interim) SWE (Dee et al., 2011), and Modern-Era Retrospective Analysis for Research and Applications Version 2 (MERRA-2) SWE (Gelaro et al., 2017).

However, in addition to the above-mentioned advantages, different SWE products have disadvantages in terms of uncertainty and incompleteness. The uncertainty of satellite-based products is mainly attributed to topographic and climatic factors (Chang et al., 1996; Derksen, 2008), and that of reanalysis and data assimilation products is partly attributed to several structural errors and inputs of in situ data, such as altitude bias caused by spatial differences between grids and sites (Dutra et al., 2011; Reichler and Kim, 2008). Regarding data incompleteness, due to the limited detection capability of passive microwaves in mountainous regions, GlobSnow SWE only provides terrestrial non-mountainous regions of the Northern Hemisphere between latitudes 35°–85° N, excluding glaciers and Greenland (Luojus et al., 2021). In addition, the time series of the AMSR-E/AMSE2 SWE ranges from 2003 to 2022 (Imaoka et al., 2010; Kelly, 2009; Tedesco and Jeyaratnam, 2019). Moreover, existing SWE products are inconsistent with each other and show diverse spatiotemporal patterns. A comparison of five SWE gridded products (GlobSnow, GLDAS, ERA-Interim/Land, MERRA, and Crocus SWE (Brun et al., 2013)) throughout the Northern Hemisphere was conducted by Mudryk et al. (2015), showing that the consistency of five products is only approximately 50 % in the climatological peak snow mass. As a result, these datasets exhibited exceedingly distinct SWE trends, where Crocus, ERA-Interim/Land, and MERRA SWE showed stronger negative SWE trends than GlobSnow, and GLDAS showed much weaker trends than the other four datasets. Yang et al. (2020a) found that both AMSR2 and GlobSnow-2 SWE show overestimation in China, and their gap in validated bias reached approximately 20 mm.

Against this backdrop, previous studies have attempted to improve the accuracy of SWE estimates by fusing multisource gridded products, considering that different SWE products have advantages and could be complementary to each other, such as simple arithmetic average models (Mudryk et al., 2015) and multiple linear regression models (Snauffer et al., 2018). Unfortunately, these linear models have some deficiencies, which usually tend to overfit SWE and are unable to take advantage of different products. Machine learning methods hold advantages in modeling more complex patterns and have achieved great success in the fusion of climatological variables (Baez-Villanueva et al., 2020; Ma and Liang, 2022; Shao et al., 2022; Snauffer et al., 2018; Wei et al., 2021, 2022). A few studies applied machine learning models to fuse multisource SWE products, such as the ridge regression model (Shao et al., 2022) and the random forest model (Hu et al., 2021), which show advantages in handling nonlinear relations between SWE and its influencing factors relative to linear fusion models. However, these fusion models usually use geographical coordinates as spatial predictors to describe geospatial information, which usually causes unnatural surfaces in mapping, such as irregular circular arcs (Behrens et al., 2018; Hengl et al., 2018). Therefore, more suitable geospatial and temporal features should be introduced to construct SWE fusion models concerning the spatiotemporal heterogeneity in SWE.

Extreme gradient boosting (XGBoost) is an ensemble learning method and has achieved great success in diverse applications, particularly in climatological variable estimation, as demonstrated in previous studies (Bentéjac et al., 2021; Chen et al., 2019). XGBoost uses a scalable ensemble of unpruned decision trees and improves predictive performance, making it a hybrid of the gradient boosting and random forest approaches, and achieving the superiority in controlling overfitting, regularized boosting, and parallel processing (Fan et al., 2018; Karthikeyan and Mishra, 2021). Accordingly, XGBoost holds great potential to fuse SWE products, spatiotemporal covariates, and in situ observations by learning widely from various SWE products and handling nonlinear relations between SWE and its factors.

In this study, we aim to establish a spatiotemporal fusion model capable of improving daily SWE estimates with a spatial resolution of 25 km, which can alleviate the problems of SWE data uncertainty and incompleteness. The main objectives are (1) to develop an XGBoost fusion model by integrating three types of SWE products with relatively spatiotemporal continuity, moderate accuracy against in situ observations, including GlobSnow, ERA-Interim, ERA5-Land, GLDAS, and CSWE (a spatiotemporal resolution of daily, < 25 km); (2) to propose a series of geospatial and temporal features for capturing the spatiotemporal heterogeneity of SWE, such as Geo-space codes and Snow-DOY; and (3) to derive daily SWE products from 1980 to 2020 using the proposed model and to assess the spatiotemporal characteristics of SWE in China.

2. Study area and data

2.1. In situ SWE

Located in East Asia between 73°–135° E and 10°–53° N, China comprises 19 % of the Northern Hemisphere's snow cover area (Armstrong and Brodzik, 2001; Hori et al., 2017; Pulliainen et al., 2020), especially in Northeast-Inner Mongolia (NIM), Xinjiang (XJ) and the Qinghai-Tibetan Plateau (QTP). These areas are the three most stable seasonal snow cover areas of China, including 27 % of the snow-covered areas of the country in winter from 2000 to 2014 (Huang et al., 2016). Daily ground-measured snow pressure (g/cm^2) data from snow volume gauge or snow pillow at 647 sites (Fig. 1) across mainland China from 1 January 2013 to 31 December 2017 are collected from the China Meteorological Administration (CMA, 2003). The maximum and mean values of in situ SWE in China and its three snow cover areas are calculated to explore the snow situation of the 5 years, as shown in Table 1. In total, 13,785 valid in situ SWE samples (80 % of them come from 122 sites) are generated from daily ground-measured snow pressure data to train and validate the proposed model.

2.2. SWE data and covariates

Given the respective advantages of different SWE products, five state-of-the-art gridded SWE products are adopted for fusion, including GlobSnow, ERA-Interim, ERA5-Land, GLDAS, and CSWE. Specifically, the selected data assimilation SWE products include GlobSnow and GLDAS. The GlobSnow was issued by the European Space Agency, which combined daily snow depth data, ground-measured data, and satellite microwave radiometer data through snow-condition correction (Luojus et al., 2021). GLDAS is a model incorporating satellite-based and ground-based observations to produce optimal fields of land surface states and fluxes in near-real time (Rodell et al., 2004). The ERA-Interim and ERA5-Land belong to reanalysis SWE with more integral records, where the ERA-Interim is the fourth reanalysis product generated by the

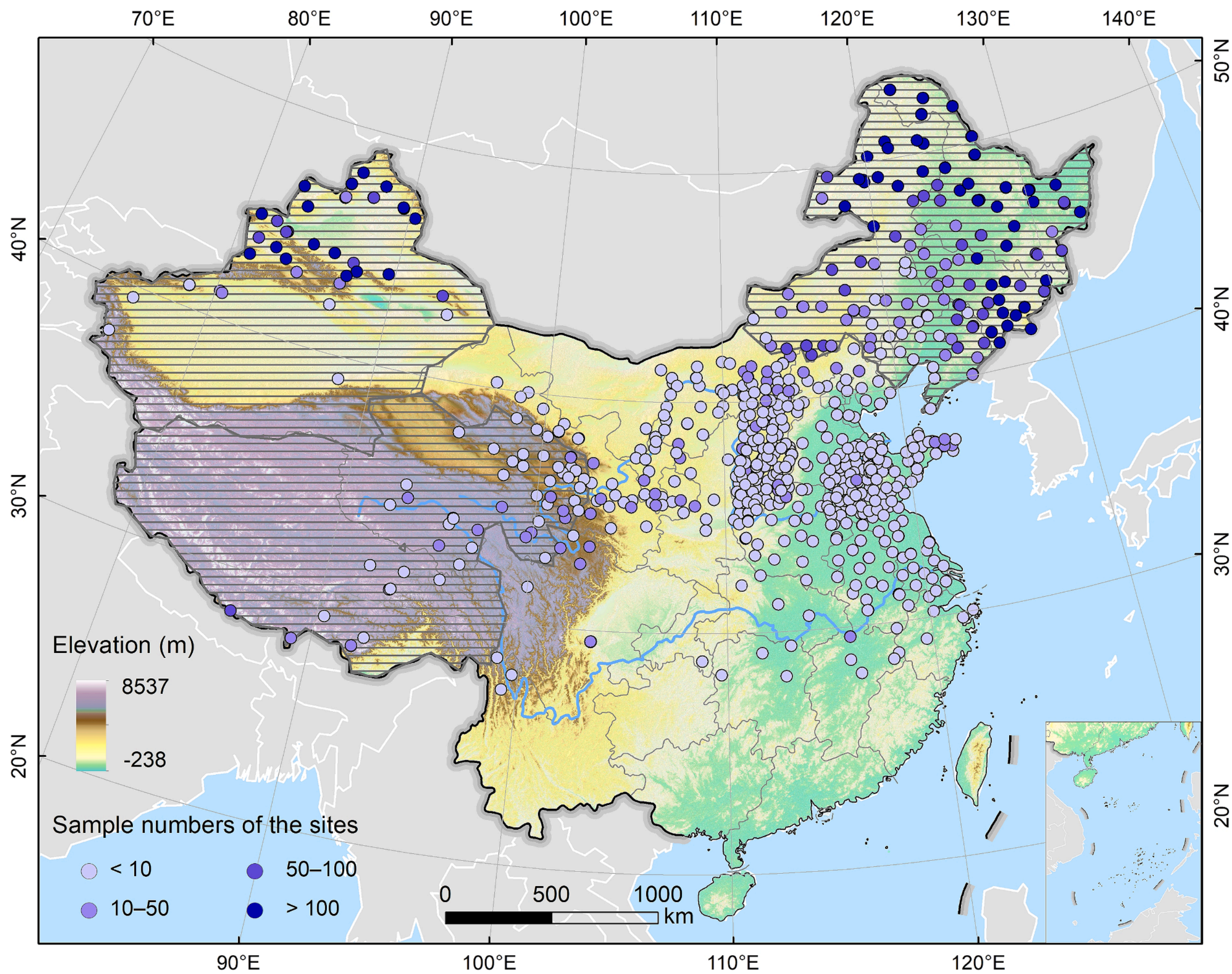

Fig. 1. Spatial distribution of the in situ SWE sampling sites in China.

Table 1
Maximum and mean values of in situ SWE in China and its three snow cover areas.

Year	Total		NIM		XJ		QTP	
	max	mean	max	mean	max	mean	max	mean
2013	179.00	26.84	112.00	27.66	144.00	39.46	62.00	15.46
2014	119.00	20.87	102.00	22.80	119.00	26.67	53.00	11.19
2015	170.00	18.29	121.00	15.66	146.00	25.96	24.00	9.19
2016	140.00	20.79	140.00	16.31	99.00	33.82	25.00	9.61
2017	172.00	21.93	69.00	17.49	124.00	37.52	55.00	9.17

ECMWF, which is assimilated by multisource land surface, oceanographic, and space-borne measurements, based on the Integrated Forecast System (Dee et al., 2011). ERA5-Land has made several parameterization improvements and corrections to precipitation data in the land surface model compared with ERA-Interim dataset, making it more suitable for hydrological research (Balsamo et al., 2015; Muñoz-Sabater et al., 2021). In addition, the satellite-based CSWE product generated by a linear unmixed method through a passive microwave radiometer is employed, which was proven to be more suitable for SWE estimation in China (Jiang et al., 2022).

The nonlinear relations between SWE and temperature, vegetation, and terrain may not be fully expressed by a single SWE product alone because different SWE estimation schemes consider distinct influential factors. For example, CSWE considers land use types, and GlobSnow focuses on non-mountainous areas. As a consequence, snow-related, land cover, 2-m air temperature, and elevation covariates are embedded in our model to explain the nonlinear interrelations between SWE and its influential factors. The snow-related data include snow depth data (Che et al., 2016) and long-term Advanced Very High Resolution Radiometer (AVHRR) snow cover extent (SCE) data (Hao et al., 2021). Based on the SCE data, we calculate the snow cover onset date (SCOD) and snow cover end date (SCED) to indicate the duration of snow in a certain hydrological year, avoiding the impact of temporary snow cover (Chen et al., 2015; Sun et al., 2020; Wang et al., 2022). The land cover data with 1-km resolution are obtained from the Data Center for Resources and Environmental Sciences, and the temperature data are from ERA5-Land. In addition, the Shuttle Radar Topography Mission Digital Elevation Model (DEM) with 90-m resolution is used to extract topological features. Table 2 summarizes the descriptions of the data used in the study, and all the gridded data are resampled to an identical spatiotemporal resolution (daily, 25 km).

Table 2
Summary of the data sources for the fusion model.

Data	Time range	Temporal resolution	Spatial resolution	Acquisition link
GlobSnow	1979–2018	daily	0.25°	https://www.globsnow.info
ERA-Interim	1979–2019	6-hourly	0.25°	https://www.ecmwf.int
ERA5-Land	1981–	hourly	0.1°	https://cds.climate.copernicus.eu
GLDAS	2003–	daily	0.25°	https://disc.gsfc.nasa.gov
CSWE	1980–2020	daily	25 km	https://www.scidb.cn/en
Snow depth	1980–2020	daily	25 km	https://poles.tpdc.ac.cn
AVHRR SCE	1980–2020	daily	5 km	https://www.ncdc.ac.cn
Temperature	1981–	hourly	0.1°	https://cds.climate.copernicus.eu
Land cover	–	–	1 km	https://www.resdc.cn
DEM	–	–	90 m	https://earthexplorer.usgs.gov

3. Methodology

3.1. Input features to the fusion model

There are six categories of features in the proposed fusion model for a total of 36 features, as shown in Table 3. The reasons for selecting the features are illustrated as follows.

The fused SWE products should fulfill the following conditions: (1) covering satellite-based, data assimilation, and reanalysis SWE types, which could be complementary to each other and lead to a full fusion of various types of products, (2) having relatively spatiotemporal continuity, moderate accuracy against in situ observations, and (3) with a spatiotemporal resolution of daily, $<$ 25 km. Among all available SWE products, GlobSnow, ERA5-Land, ERA-Interim, GLDAS, and CSWE are selected, according to evaluation results in existing studies (Che et al., 2016; Dai et al., 2012; Yang et al., 2019).

Land cover types have usually been considered to improve SWE retrieval algorithms (Chang et al., 2009; Derksen et al., 2005), mainly because different land cover types will affect the aggregation and distribution of snow. For example, forest canopies intercept snow accumulation, and bare land typically has shallow snow (Jiang et al., 2014). Thus, China Land Use Land Cover Remote Sensing Monitoring Data Set (CNLUCC) (Xu et al., 2018) are considered to reflect the heterogeneous influence of land cover on SWE. In addition, the temperature feature is involved in our model because snow storage, replenishment, and melt are mainly controlled by temperature. Additionally, since the radiation and thermal conductivity characteristics of snow are highly related to snow depth and snow cover duration (Li and Mi., 1983), the snow-related features of snow depth, SCOD, and SCED are adopted. In particular, the geospatial and temporal features are introduced to depict the spatiotemporal heterogeneity of SWE, which were not delicately considered by existing SWE fusion models.

Table 3
List of input features to the fusion model.

Category	Feature	Number of features from category
SWE products	GlobSnow, ERA-Interim, ERA5-Land, GLDAS, and CSWE	5
Land cover	CNLUCC	1
Temperature	ERA5-Land 2-m air temperature	1
Snow-related	Northern snow depth, AVHRR SCOD, and SCED	3
Time	year, month, DOY, Seasonal-DOY (D_a,D_b,D_c, D_d), and Snow-DOY (D1, D2)	9
Geo-space	Geo-space code (X, Y, and Z), mean and standard deviation of topological features (elevation, slope, aspect, plan curvature, profile curvature, Eastern, and TPI)	17

As SWE has strong temporal heterogeneity, seasonal cycle, and snow-season cycle, the temporal features in our model include not only the year, month, and day of the year (DOY) but also Seasonal-DOY and Snow-DOY. Since snow is regulated by the seasonal cycle as an earth parameter, Seasonal-DOY are used to account for the seasonal variability in SWE. Seasonal-DOY (D_a, D_b, D_c, D_d) are calculated by the inverse distances from a certain day to the middle day of four seasons (spring equinox, summer solstice, autumn equinox, and winter solstice) (Wei et al., 2022). In addition, the snow season can be roughly divided into accumulation and melting periods. The accumulation period characterizes the interaction of snowfalls leading to higher snow depth. The melting period usually shows higher liquid water due to snow melt. These snow-season characteristics also circulate in a hydrological year, called the snow-season cycle. Snow-DOY (D1, D2) are calculated by the inverse temporal distances from a certain day to SCOD and SCED, respectively, as shown in Eq. (1) and (2).

$$D1 = \frac{1}{|SCOD - DOY|} \tag{1}$$

$$D2 = \frac{1}{|SCED - DOY|} \tag{2}$$

The geospatial features consist of Geo-space code and fine topological features, which can enhance the spatial expression of the model. Usually, SWE patterns show a strong latitudinal zonality, mainly because the thermal conditions highly dominate the SWE distribution. Meanwhile, local geolocation information should be introduced to the fusion model considering SWE also has strong spatial heterogeneity. Furthermore, considering that the high-latitude grid is smaller than the low-latitude grid and a sudden value change occurs between 180° W longitude and 180° E longitude, we consequently adopt the Geo-space code (X, Y, and Z) to transform polar coordinates into Cartesian coordinates (Yang et al., 2022), as shown in Eq. (3), (4) and (5), respectively.

$$X = Rsin\theta cos\varphi \tag{3}$$

$$Y = Rsin\varphi \tag{4}$$

$$Z = Rcos\theta cos\varphi \tag{5}$$

where R is the earth's radius; θ is the longitude; and φ is the latitude.

The distribution of SWE and the accumulation and melting of snow are partly controlled by the interactions between the atmosphere and local topography, especially in mountain areas (Essery and Pomeroy, 2004; Sturm and Wagner, 2010; Trujillo et al., 2007). However, the spatial resolution of existing gridded SWE products is approximately 25 km, and it is difficult to describe complex terrain under such coarse resolution. Thus, we first calculate the topological features based on a 90-m DEM, on which we calculate the mean and standard deviation of each feature within a 25 km × 25 km grid to indicate the local topography for each grid.

Among the topological features, elevation is the key indicator of SWE accumulation and melting (Anderton et al., 2004). However, the use of elevation alone cannot accurately reflect the interaction between SWE and the environment in local regions. As a result, the features of the slope, aspect, plan curvature (Cur1), profile curvature (Cur2), Eastern (Vafakhah et al., 2022), and TPI (Ganjkhanlo et al., 2020; Meloche et al., 2022) are further involved to delicately reflect the physical contexts on a regional scale. In particular, the Eastern usually has a negative impact on SWE, which reflects receiving solar energy and influences snowmelt. TPI provides the height information of each pixel relative to surrounding pixels and thus explains the redistributive impact of wind on SWE.

3.2. Spatiotemporal XGBoost model

The XGBoost model, advanced by the gradient boosting decision tree, has abundant trees to build a strong boosted classifier by employing an ensemble of weak classifiers. XGBoost has been recursively used to estimate surface attributes when working with remote sensing data (Chen et al., 2019; Just et al., 2018; Karthikeyan and Mishra, 2021) because it has great potential in modeling complex nonlinear relations and handling large unbalanced datasets. The superiority of XGBoost model derives from the improvement of training and prediction efficiency, being highly robust to outliers and computationally lighter than other methods (Chen and Guestrin, 2016; Friedman, 2001). Therefore, XGBoost is identified as an appropriate model for fusing multisource datasets with strong nonlinear relations to improve SWE estimates.

Based on the XGBoost model, we add spatiotemporal features explaining the heterogeneity of SWE to construct a spatiotemporal XGBoost model. The schematic of the spatiotemporal XGBoost model is shown in Fig. 2. The user-defined parameters are optimized by grid search and cross-validation, as shown in Table 4. The number of trees refers to the number of weak classifiers. The learning rate indicates the shrinkage of the iterative decision tree. The regularization techniques included in XGBoost are the maximum depth of the tree (max_depth), the minimum weight needed for a leaf node (min_child_weight), the subsampling rate (subsample), the fraction of features to be evaluated at each split (colsample_bytree), the minimum loss reduction (gamma), and the regularization degree (reg_alpha), which are used to control the complexity of the model, increase the training speed, and reduce overfitting (Bentéjac et al., 2021).

We use the K-fold cross-validation strategy to train and validate the model, which is suitable for small samples through its advantage of repeatedly using randomly generated subsamples for training and validation at the same time. According to the principle of a K-fold cross-validation technique (Rodriguez et al., 2010), the samples are divided into K subsets independently, one of the subsets for model validation in turn and the others for model fitting. This process should circulate K times, and K validation results would be obtained. All the K-fold results are summarized to evaluate the model performance, which can reduce bias derived from a specific validation set and thus reduce overfitting and obtain a more robust model. For example, annual cross-validation entails using samples from each year as a fold and site cross-validation involves using samples from each site as a fold. It is noted that there are 647 sites but 80 % of samples come from 122 sites, indicating an uneven distribution of sample numbers across sites. Additionally, strong spatial auto-correlation exists among SWE and its spatiotemporal covariates. Considering these uneven sample distributions and embedded spatially auto-correlated structures, site cross-validation (or site leave one out cross-validation) is more suitable for spatial assessment of model. It offers precise model assessment by using each site samples as an independent validation set, minimizing reliance on any individual site validation. Although site cross-validation is more sensitive to overfitting compared with fewer-fold cross-validation, it mitigates the need for intricate and unexplained spatial sampling partitions, making it better suited for spatially auto-correlated data. Specifically, we conduct SWE accuracy evaluations using ground measurement data from 2013 to 2017 based on the annual and site cross-validation strategy to validate the spatiotemporal prediction of the model. Three statistical indicators, i.e., mean absolute error (MAE, mm), root mean square error (RMSE, mm), and Pearson correlation coefficient (R), are adopted to quantitatively evaluate the model performance.

Table 4
List of the optimized hyperparameters.

Hyperparameter	Value
Number of trees	60
Learning rate	0.17
Max_depth	5
Min_child_weight	5
Gamma	0
Subsample	0.8
Colsample_bytree	0.5
Reg_alpha	0.05

4. Results

4.1. Overall accuracy

We first investigate the effectiveness of input features on model performance, as indicated by feature importance of the trained XGBoost model based on mean decreased accuracy. As shown in Fig. 3(a), the five SWE products account for 32.8 % of feature importance, within which ERA5-Land and CSWE are the most important. The covariates account for 67.2 % of feature importance, highlighting important roles played by covariates in the model. Among the covariates, geospatial features reach the highest importance, followed by snow-related features. It is noted that the *Z* coordinate represents the distance of a point on the ideal sphere from the earth center rather than actual elevation. This

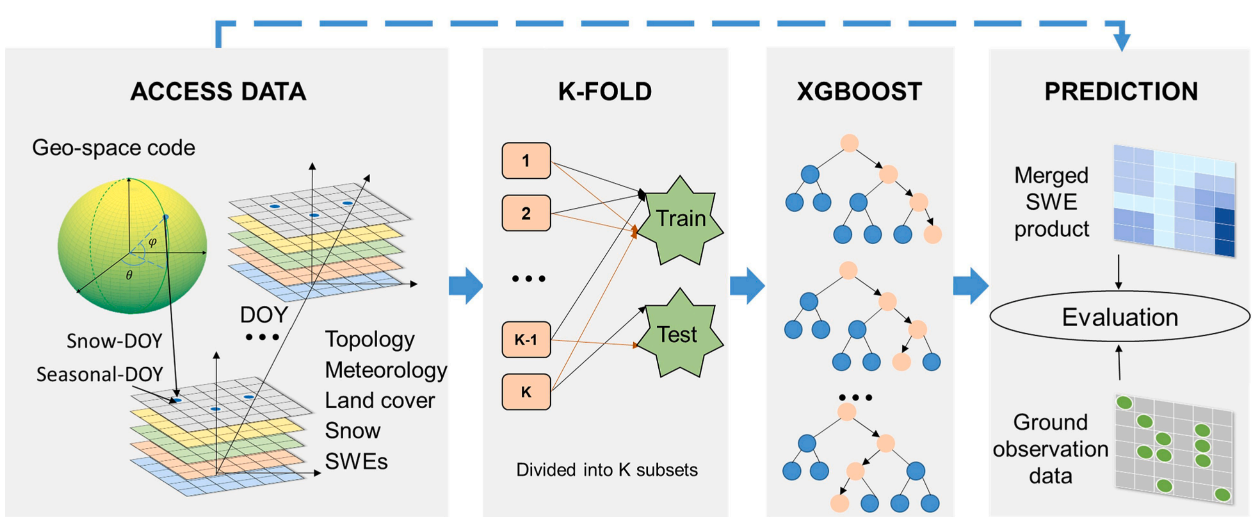

Fig. 2. Flowchart of the spatiotemporal XGBoost fusion model, which improves the accuracy of SWE estimation from the combination of SWE products, spatiotemporal features, and ground observation data.

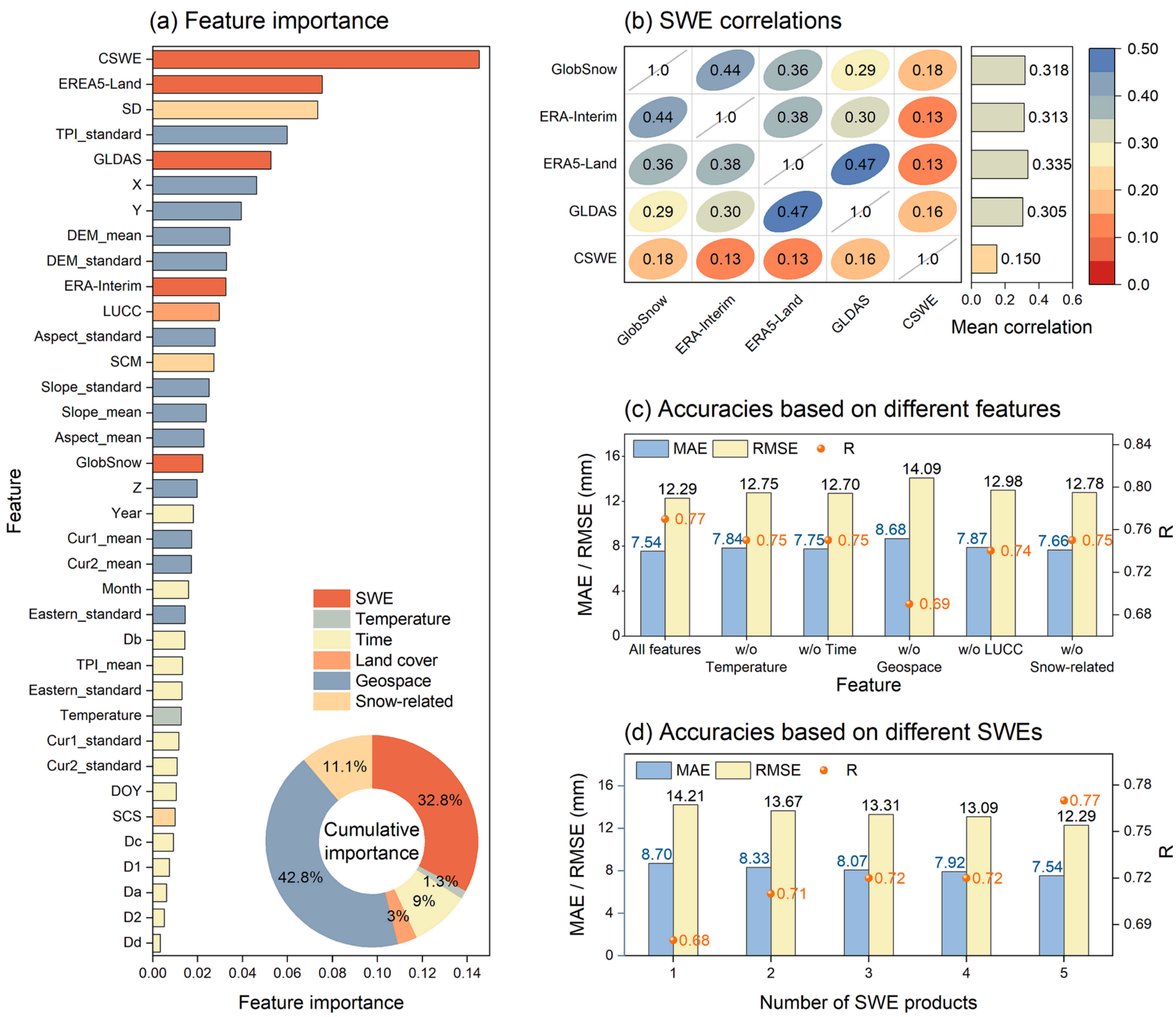

Fig. 3. Feature importance in the spatiotemporal XGBoost model. (a) Feature importance scores and the cumulative feature importance, (b) correlations between member SWE products, (c) model accuracies with different input features, in which w/o means without inputting the feature into the model, and (d) model accuracies with different combinations of member SWE products.

distinction may lead to a relatively higher importance score of *X* and *Y* coordinates compared to *Z* coordinate. As shown in Fig. 3(c), all features can improve SWE estimation, and the geospatial features make the largest contributions to improving accuracy, followed by the land cover feature.

We then calculate the pairwise correlation between each pair of products and the mean correlation for each product, as shown in Fig. 3 (b), reflecting the poor consistency between member SWE products with mean correlations of individual products smaller than 0.34. We further compare the accuracies of the spatiotemporal XGBoost model with different combinations of SWE inputs to analyze the advantage of fusing multisource SWE products, as shown in Fig. 3(d). Totally, there are 31 possible combinations of any number of products, and the average accuracy of the same number of combination results is calculated for the sake of presentation, i.e., we use each/2/3/4/all of five products as SWE input and calculate the average accuracy of the 5/10/10/5/1 results. It is noted that the spatiotemporal covariates remain the same for the comparison, so that the accuracy difference would directly reveal the influence of different SWE inputs. Generally, the accuracies continuously increase with more member products involved and reach the best with all five products as SWE input. Compared with single-product fusion, the MAE was reduced by 13.3 %, the RMSE was reduced by 13.5 %, and the R was increased by 13.2 % when fusing five SWE products.

The comparison of the accuracies of XGBoost SWE and member products shows that the XGBoost SWE based on both annual and site cross-validation achieves apparently higher accuracy with improved regression lines (Fig. 4), demonstrating the prediction ability of the spatiotemporal XGBoost model. Compared with the member products, the accuracy of the XGBoost SWE decreases the MAE and RMSE from 12.90 to 18.21 mm to 7.54, 8.62 mm and from 19.02 to 25.27 mm to 12.29, 13.73 mm, respectively, and increases the R from 0.36 to 0.51 to 0.77, 0.70, respectively. Except for the XGBoost SWE, the accuracy of CSWE is higher than that of the other products, with an R of 0.49, a MAE of 13.12 mm, and an RMSE of 19.02 mm. In addition, the high-density areas of the GLDAS and ERA-Interim deviate from the 1:1 line and show an apparent underestimation of SWE, while GlobSnow and ERA5-Land show markedly overestimated SWE.

4.2. *Accuracies at different temporal scales*

Each SWE product in each month, season, and year from 2013 to 2017 is evaluated against in situ observations, and these accuracies are summarized in months, seasons, and years to provide insight into the temporal stability of the model performance, as shown in Fig. 5. At the annual scale (Fig. 5a1-a3), the accuracy of the XGBoost SWE based on

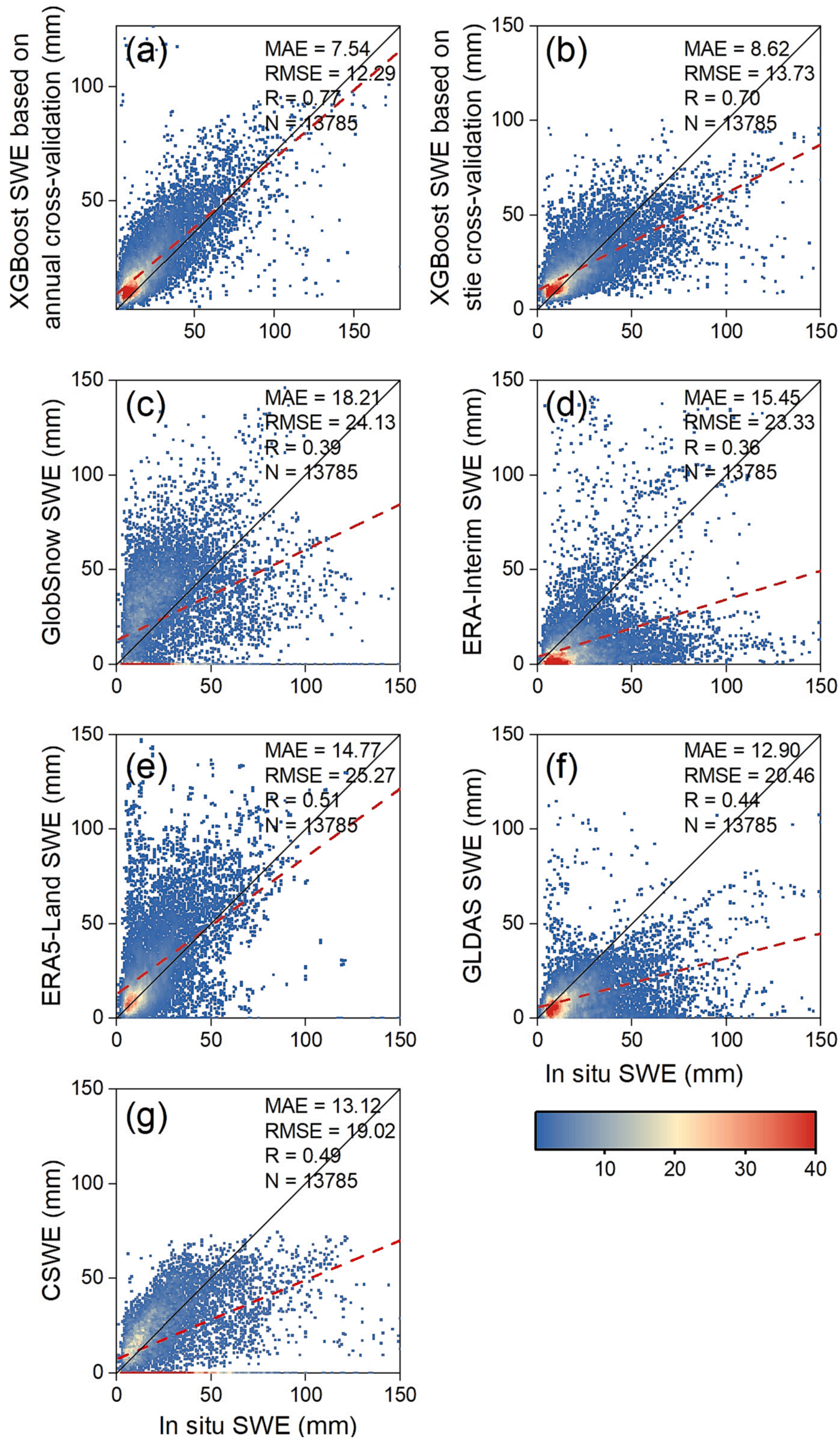

Fig. 4. Accuracies of the proposed XGBoost SWE and the five-member SWE products over China. N means the number of samples. The black solid and red dashed lines represent the 1:1 line and the linear regression line, respectively. The color bar represents the value of the kernel density estimation.

annual cross-validation is stable in all years, showing the highest stability, with a mean MAE, RMSE, and R of 7.47 mm, 12.16 mm, and 0.77, respectively. At the seasonal scale (Fig. 5b1-b3) and the monthly scale (Fig. 5c1-c3), XGBoost SWE outperforms existing products in all seasons and months, as evidenced by metric values.

Furthermore, we analyze the performance of XGBoost SWE in each season and month to reveal the effectiveness of the XGBoost model in different seasons and months, as shown in Fig. 6. The model achieves the best estimation performance in winter, with a MAE of 7.28 mm, an RMSE of 11.77 mm, and an R of 0.79. Within winter, the highest accuracy appears in December as a result of the stable snow state and relatively sufficient observation samples. The accuracies in spring and

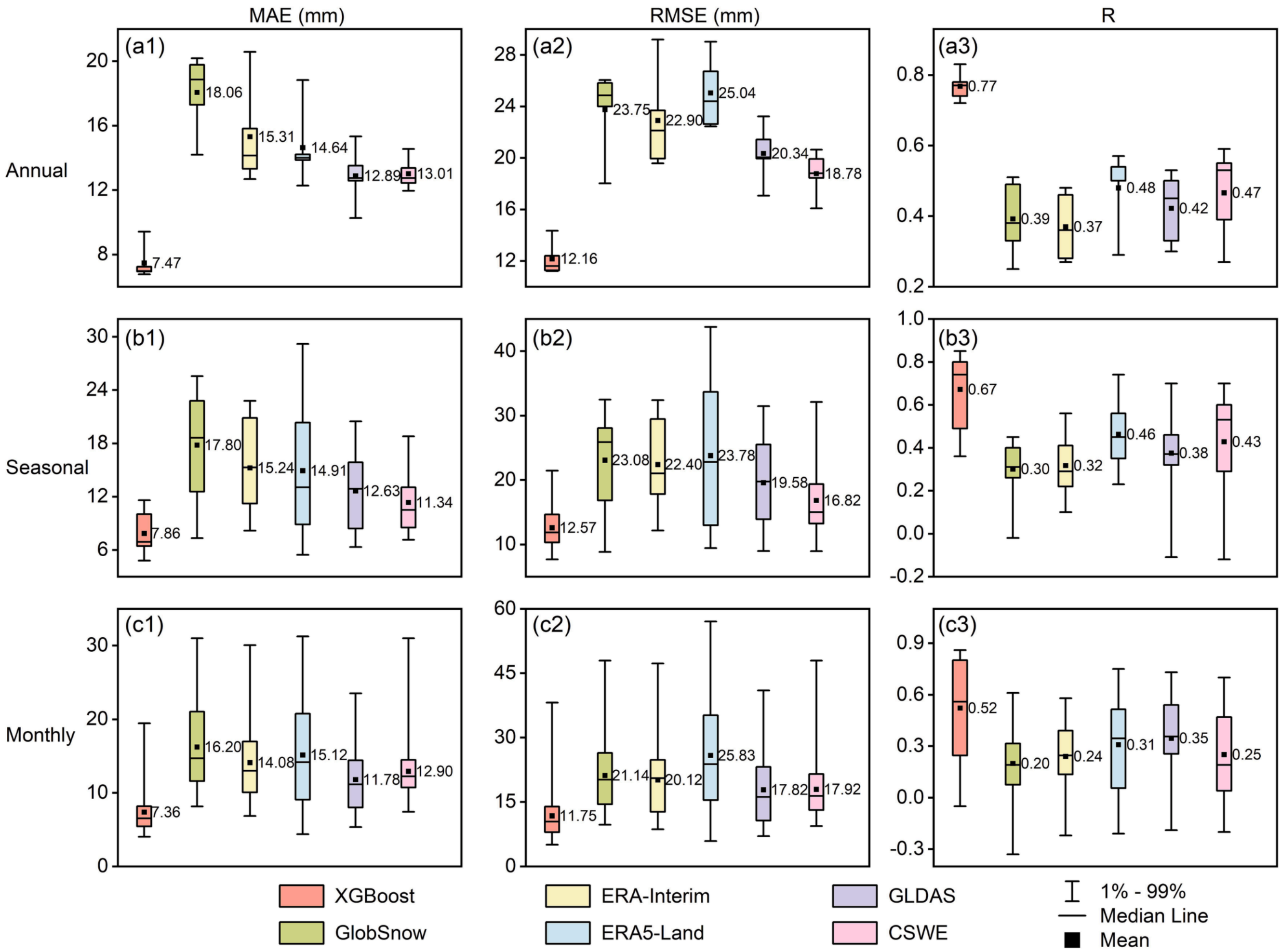

Fig. 5. Accuracies of the XGBoost SWE and the five-member SWE products at different temporal scales: the yearly MAE (a1), RMSE (a2), R (a3); the seasonal MAE (b1), RMSE (b2), R (b3); and the monthly MAE (c1), RMSE (c2), R (c3).

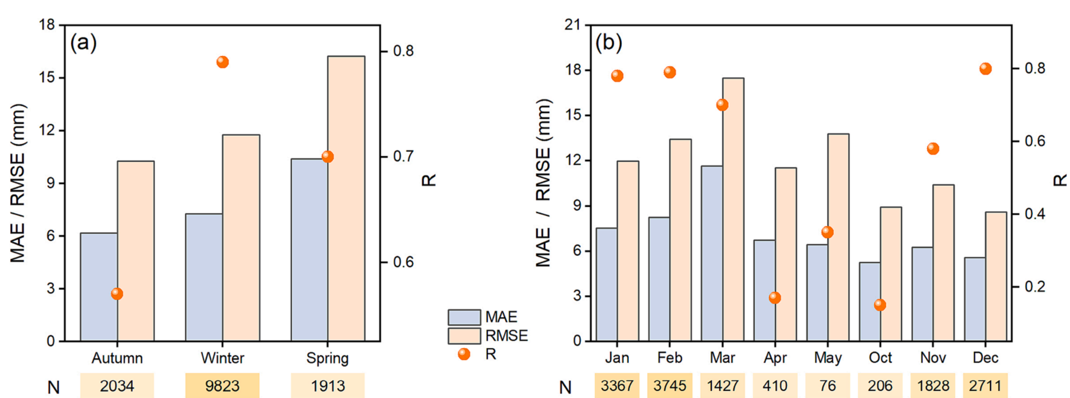

Fig. 6. Accuracies of the XGBoost SWE in different seasons (a) and months (b). N means the number of samples.

autumn are inferior to those in winter, which is mainly attributed to the relatively rapid changes in snow as well as the fewer observations, especially in October, April, and May.

4.3. Accuracies at different locations

Due to the considerable variability of the climate and topography over China, SWE presents high spatial heterogeneity. SWE accuracies in different snow cover areas and different elevations are evaluated to investigate the performance of the proposed model in spatial contexts (Fig. 7).

XGBoost SWE based on annual cross-validation achieves the best accuracy in all areas. In XJ with the most snow accumulation and in NIM with relatively flat topography and intermediate snow accumulation, the XGBoost SWE exhibits the highest R values of 0.80 and 0.75 due to the abundant samples and thus excellent fusion performance. The XGBoost SWE exhibits an apparently lower R of 0.40 in QTP than in XJ and NIM but the best MAE and RMSE. In addition to the spatiotemporal

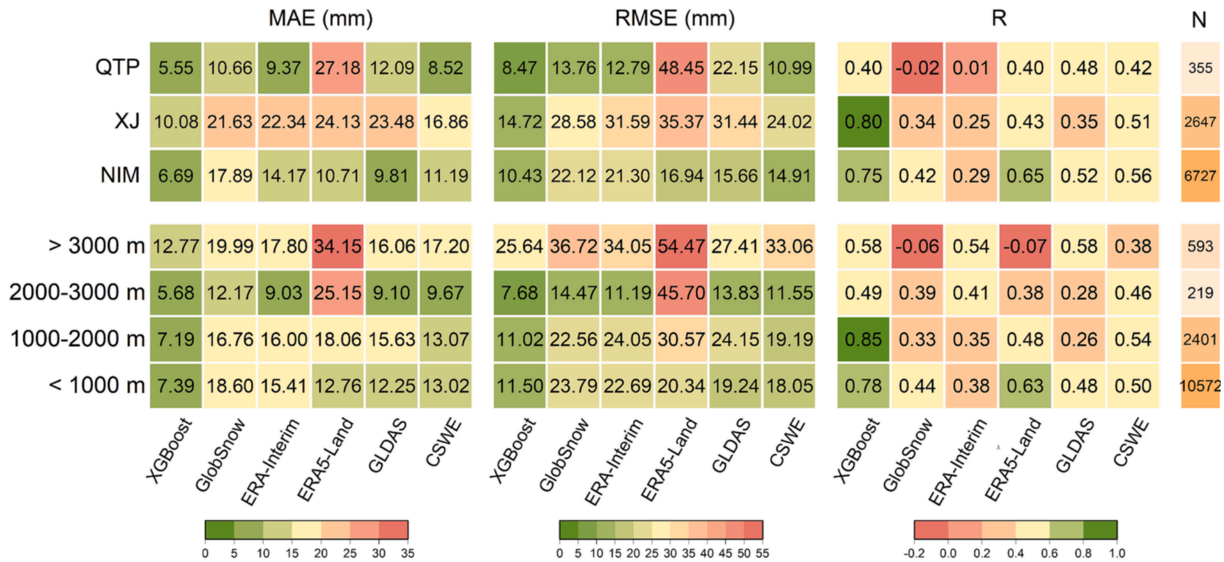

Fig. 7. Accuracies of the XGBoost SWE and the five-member SWE products in three snow cover areas and four elevation ranges. N means the number of samples.

heterogeneity of SWE, the QTP has the smallest number of observation samples (355) and thus the most uneven distribution of samples, which may result in poorer performance in QTP than in XJ and NIM. Moreover, the very low R of GlobSnow (–0.02) and ERA-Interim (0.01) could be another reason for the relatively low R of XGBoost SWE in QTP because ERA-Interim and GlobSnow play moderate roles in XGBoost model. Although the R of XGBoost SWE in QTP is relatively lower than GLDAS and CSWE, the MAE and RMSE of XGBoost SWE in QTP are the lowest among all products.

The accuracies at different elevations (Fig. 7) show that XGBoost model can improve SWE estimation in every elevation range. XGBoost SWE surpasses all products with MAEs of 5.68–7.39 mm, RMSEs of 7.68–11.50 mm, and R of 0.49–0.85 at elevations lower than 2000 m, showing an apparent improvement in estimation due to the abundant samples. For elevations higher than 2000 m, XGBoost SWE shows relatively flatter improvement due to insufficient samples. It is noted that GlobSnow and ERA5-Land exhibit negative R values of –0.06 and –0.07 as member products over 3000 m elevation, which may bring uncertainty in estimation. Apart from XGBoost SWE, GLDAS agrees well with in situ SWE over 3000 m elevation with a MAE of 16.06 mm, an RMSE of 27.41 mm, and an R of 0.58.

4.4. Spatiotemporal characteristics of the SWE over China

We derive the daily SWE product from 1980 to 2020 in China using the spatiotemporal XGBoost model, which is further masked by the AVHRR SCE data and CSWE to remove the non-snow pixels (Hao et al., 2021; Jiang et al., 2022). The mean spatially distributed multiyear maximum SWE (SWE_{max}) of the XGBoost SWE and the member SWE products in hydrological years (from September to August of the next year) are compared in Fig. 8. The changing trend (a significance level exceeding 95 %) within the time range of each product is calculated in Fig. 9. Moreover, the average SWE_{max} and its changes in different snow cover areas are calculated and shown in Fig. 10 to clearly reveal product differences.

On the one hand, XGBoost SWE product shows that the higher SWE values are mainly distributed in three stable snow cover areas, especially in mountainous areas, as shown in Fig. 10(a). Similarly, most member products show high values in NIM and XJ, contributing to the high fused values of XGBoost SWE in NIM and XJ. However, these member products show very large inconsistencies in QTP, where ERA5-Land and GLDAS show abnormally high values and ERA-Interim and CSWE show apparently lower values, as shown in Fig. 8 and Fig. 10(a). After fusion, XGBoost SWE comprehensively represents the mean status of the member products.

On the other hand, the multiyear SWE_{max} varies greatly across different products, as shown in Fig. 8. ERA5-Land and GlobSnow overestimate SWE, while GLDAS and ERA-Interim show large underestimations, similar to the results in Fig. 4. CSWE is most consistent with XGBoost SWE in different snow cover areas, as shown in Fig. 10(a). The difference between XGBoost SWE and member products is greater in QTP than in NIM and XJ, especially in mountainous areas, which mainly results from the large inconsistency among the member products in QTP.

The results in Fig. 9 and Fig. 10(b) show the changing trend of the XGBoost SWE and other products within the time range of each product based on the Mann–Kendall trend test. Overall, XGBoost, ERA-Interim, and CSWE mainly show a significant increasing trend, where XGBoost and CSWE are more closely aligned with each other. In contrast, ERA5-Land presents a significant decreasing trend in three stable snow cover areas. In addition, GlobSnow presents a significant increasing trend in XJ and a significant decreasing trend in other areas. GLDAS presents a significant decrease in NIM and XJ but an increase in QTP and other areas. It is fairer to compare the changing trend among XGBoost, GlobSnow, ERA5-Land, ERA-Interim, and CSWE rather than GLDAS because the time range of GLDAS is the most different from other products.

4.5. Comparison with other fusion models

We compare XGBoost with five existing fusion models, including random forest (RF) (Hu et al., 2021), support vector machine (SVM) (Liang et al., 2015), ridge regression (RR) (Shao et al., 2022), simple averaging (SA) (Mudryk et al., 2015), and multivariable linear regression (MLR) (Snauffer et al., 2018), to demonstrate the strength of the proposed spatiotemporal XGBoost model. The dataset is divided into a training set (70 %) and a test set (30 %), and the input features of the comparison models (except for SA) are consistent with XGBoost model. The parameters of the compared models are also determined by the same cross-validation strategy as that for XGBoost model.

The results in Fig. 11 show that the machine learning fusion models (i.e., XGBoost, RF, SVM, and RR) outperform the linear fusion models (i.e., SA and MLR), which demonstrates the superiority of machine learning models in capturing the spatiotemporal heterogeneity of SWE and handling nonlinear relations between SWE and its influence variables. The spatiotemporal XGBoost model shows a notable performance in terms of MAE of 4.91 mm, RMSE of 7.19 mm, and R of 0.91,

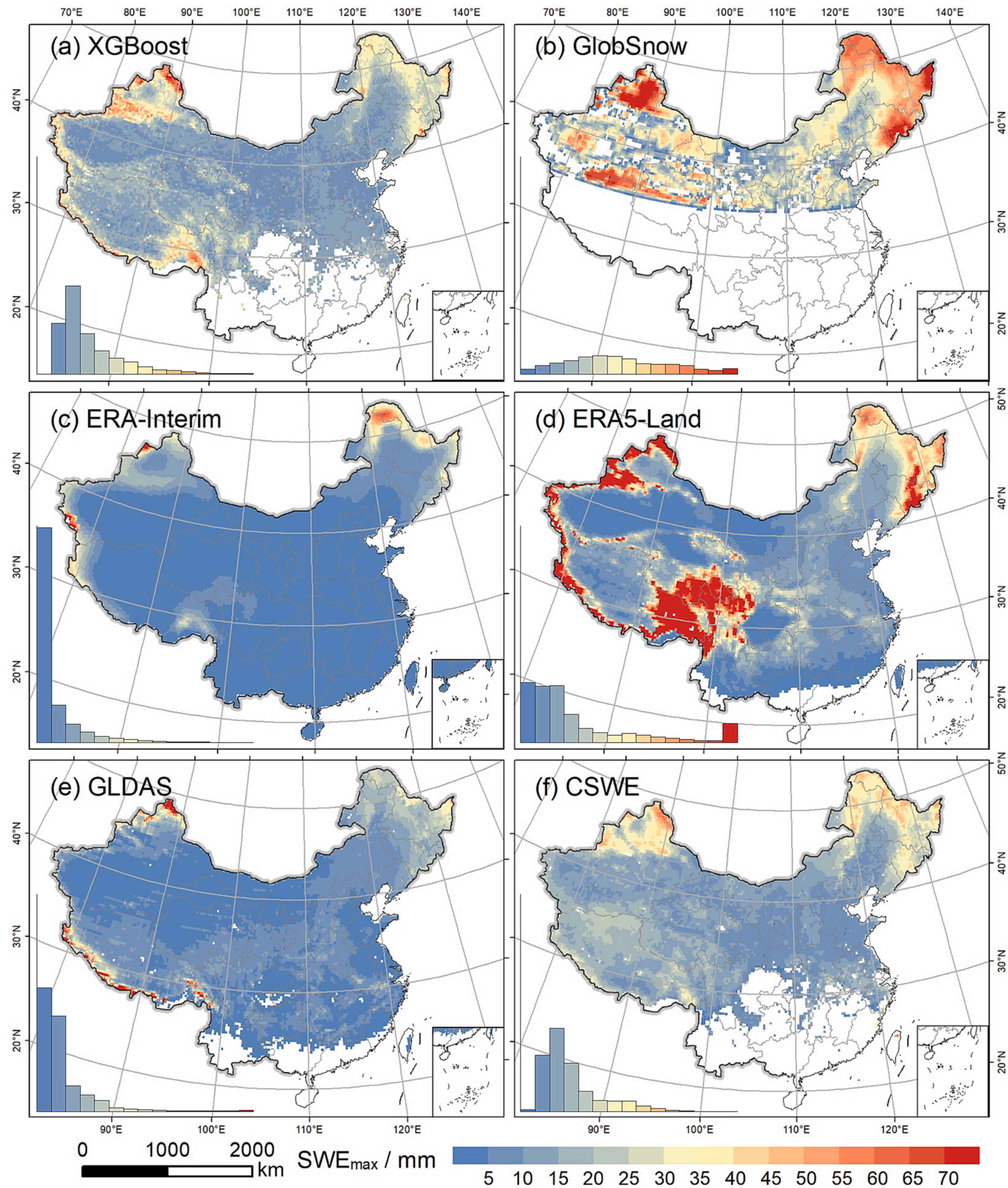

Fig. 8. Spatial distribution of the mean annual SWE_{max} of different SWE products over China.

outperforming other machine learning models and exhibiting its strength of being highly robust to outliers and computationally lighter than other methods. Among the machine learning models, RF performs the second best, with a MAE of 5.12 mm, an RMSE of 8.93, and an R of 0.90, highlighting the advantage of handling high-dimensional feature spaces.

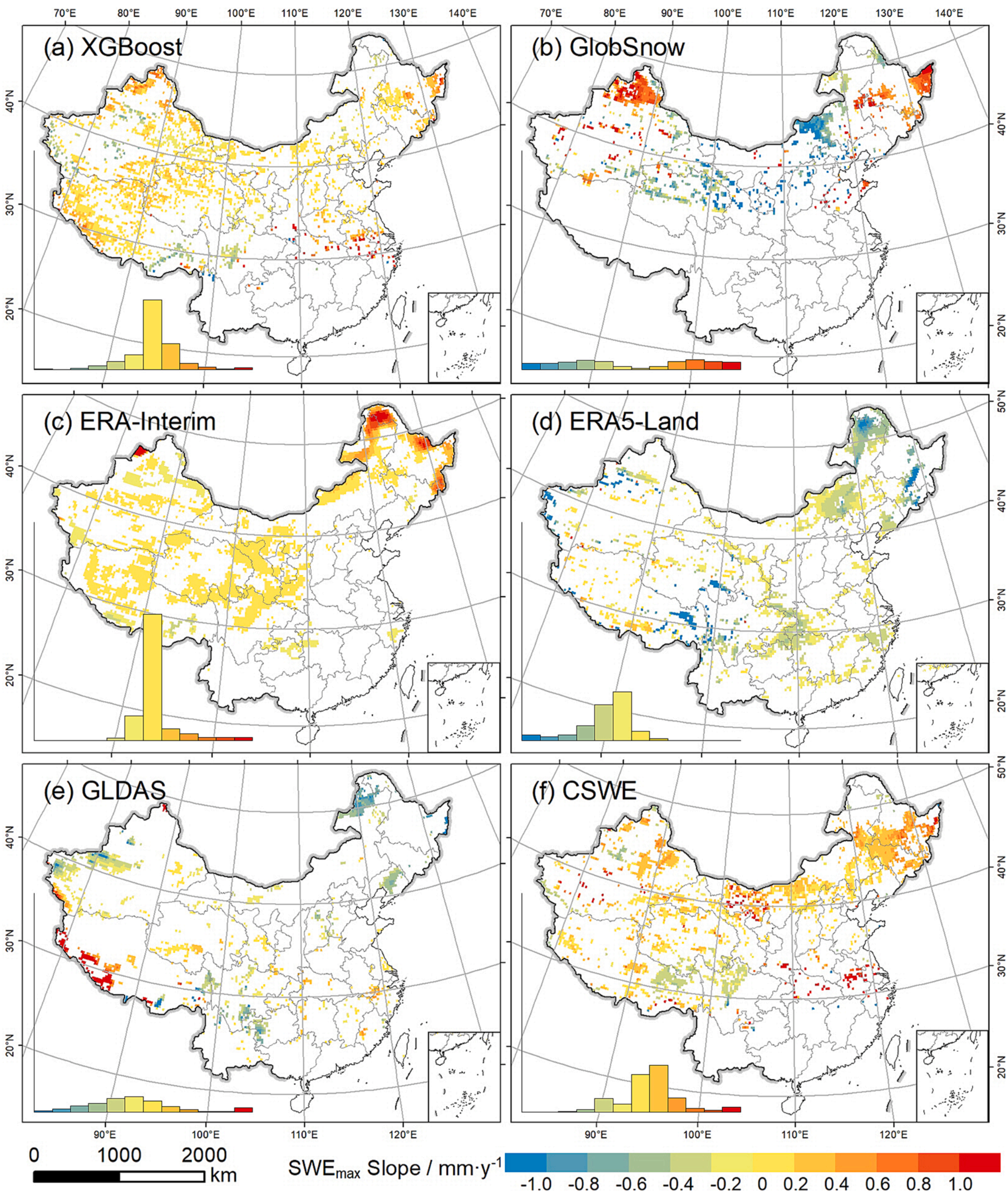

Fig. 9. Spatial distribution of annual SWE $_{max}$ change trends over China based on the Mann–Kendall trend test. Only areas with trends having a significance level exceeding 95% are shown.

5. Discussion

5.1. Effectiveness of the spatiotemporal XGBoost model

The proposed spatiotemporal XGBoost model was demonstrated to be able to derive improved SWE (see Figs. 4, 5, 6, 7, and 11), highlighting the effectiveness of the model: (1) the fusion of multisource SWE products, (2) the embedding of spatiotemporal covariates, and (3) the strong learning ability of XGBoost model to handle nonlinear relations.

All five SWE products used in spatiotemporal XGBoost model lead to the best model performance (Fig. 4d), in which CSWE and ERA5-Land are the most important features (Fig. 4a). Previous studies have illustrated the unexpected inconsistency between multisource SWEs, which may lead to different conclusions of application (Mudryk et al., 2015; Yang et al., 2020). The comparison of multisource SWE also affirms the large discrepancy in annual mean SWE_{max} and changing trends between member products (Figs. 8–9), and their correlations are under 0.36 (Fig. 4b). ERA5-Land and GlobSnow show overestimation in SWE, while ERA-Interim and GLDAS underestimate SWE (Fig. 5). Although member products have low consistency, they have respective advantages and could be complementary to each other, which aids fusion models in learning from satellite-based, assimilation, and reanalysis SWE products and thus improving SWE.

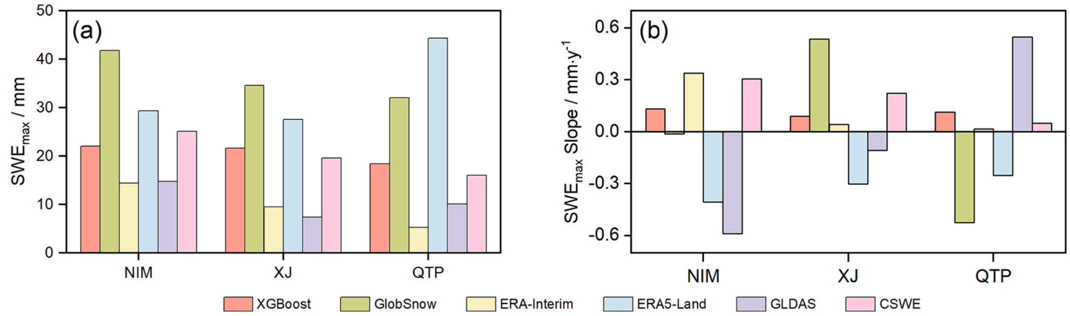

Fig. 10. Average values of annual SWE_{max} and SWE $_{max}$ trends within the stable snow cover areas.

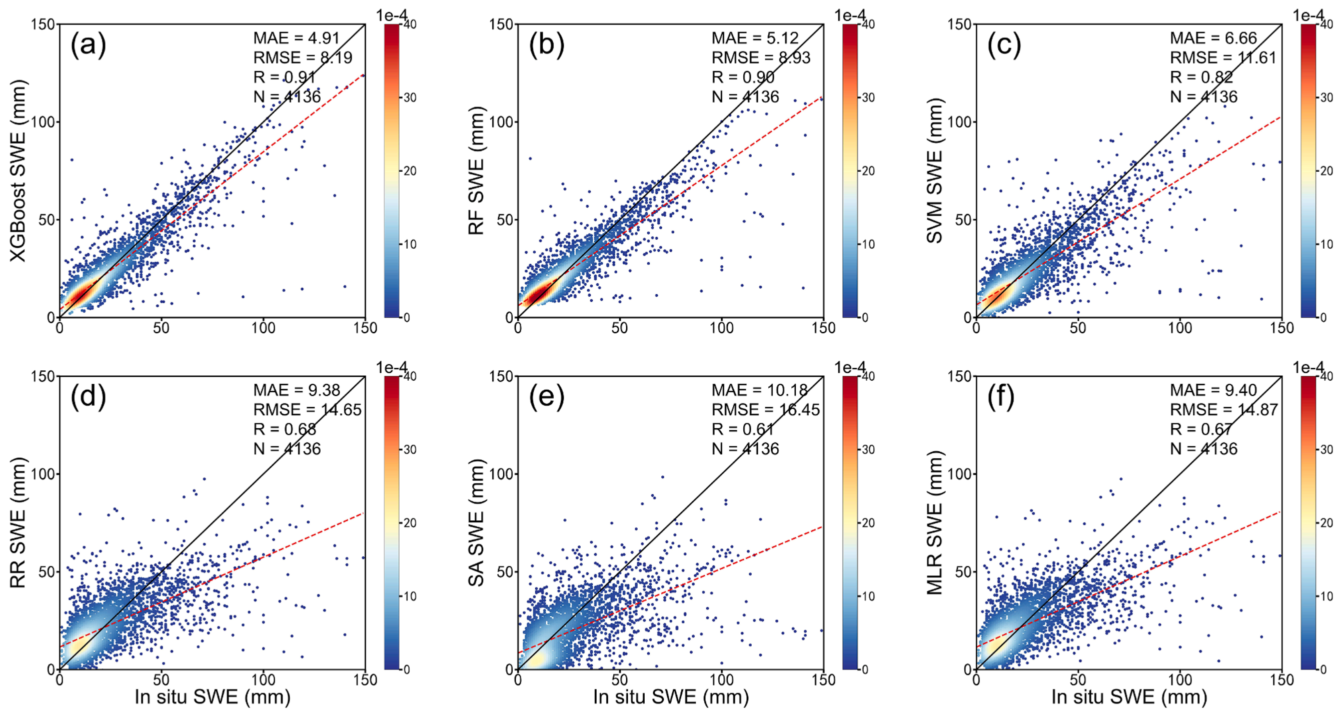

Fig. 11. Accuracy comparison among different fusion models. N means the number of samples.

The snow-related, temperature, land cover, temporal and geospatial covariates are associated with influencing factors such as snow processes, climate, underlying surface, terrain, and spatiotemporal heterogeneity of SWE. All kinds of covariates account for 67.2 % of feature importance based on the trained spatiotemporal XGBoost model (Fig. 4a), which indicates that covariates play an important role in the fusion model. These results collectively affirm the effectiveness of the model, as both the complementary SWE information and the embedded spatiotemporal covariates play important roles in improving SWE estimation.

5.2. Limitations and future prospects

Although the proposed XGBoost SWE model can take advantage of multisource SWE products and better depict the spatiotemporal characteristics of SWE, there is still room for improvement for further study.

First, the performance of the XGBoost model is partly dependent on the abundance of observation samples. The insufficient number and relatively uneven distribution of samples would result in uncertainty for the model, e.g., the model accuracy in May (samples of 76) and that in QTP (samples of 355) are inferior to other periods and regions, respectively. Second, the QTP has the most complex terrain conditions among the three stable snow cover areas in China, which poses a great challenge to SWE estimation. In addition, the performances of the member products vary in QTP: ERA5-Land and GLDAS show plentiful abnormally high values (>200 mm), while ERA-Interim and CSWE show very low values (<30 mm). It is noted that ERA5-Land is distorted in high-elevation areas possibly because ERA5-Land masks some perennial/ice-covered zones with very high SWE values (Muñoz-Sabater et al., 2021). These discrepancies are also revealed in Fig. 4 and were addressed by previous studies, such as Bian et al. (2019), Dai et al. (2017), Orsolini et al. (2019), and Yang et al. (2015). As a result, the fusion model would have higher uncertainty in the QTP than in other stable snow cover areas. Third, the uncertainty from scaling differences should not be ignored. The limited representation of in situ SWE sites makes it challenging to evaluate SWE estimates at the gridded scale.

In future studies, the incorporation of more observation samples and the utilization of more effective features or stronger machine learning models may help improve SWE estimation. For features, we will consider snow grain size, the temperature of the layer, and snow density to refer to snow physical properties, which may improve the model prediction. For models, deep learning models such as long short-term memory models and deep neural networks hold the potential to handle more complex patterns, which will be further explored. In addition, downscaling daily SWE from multisource SWE products with the fusion model would help improve the spatial resolution of SWE estimation.

6. Conclusions

We proposed a spatiotemporal XGBoost fusion model to improve the accuracy of SWE estimation by fusing multisource SWE products and spatiotemporal features. The member SWE products and spatiotemporal covariates both make great contributions to SWE estimation, especially the geospatial covariates accounting for 47.8 % of feature importance, addressing the importance of capturing spatial heterogeneity and depicting details in mapping. The effectiveness of the fusion framework was demonstrated by ground observations, achieving R values of 0.77, 0.70, MAE and RMSE values of 7.54, 8.62 mm and 12.29, 13.73 mm based on annual and site cross-validation respectively, with better performance than the member products and other fusion models. Furthermore, using the spatiotemporal XGBoost model, a dataset of daily SWE from 1980 to 2020 with 25-km resolution over China is produced, enabling us to understand the spatiotemporal patterns of SWE in China and providing accurate data for hydrological applications.

CRediT authorship contribution statement

Liyang Sun: Writing – original draft, Validation, Methodology, Data curation. **Xueliang Zhang:** Writing – review & editing, Writing – original draft, Supervision, Conceptualization. **Pengfeng Xiao:** Writing – review & editing, Conceptualization. **Huadong Wang:** Writing – review & editing. **Yunhan Wang:** Writing – review & editing. **Zhaojun Zheng:** Validation.

Declaration of competing interest

The authors declare the following financial interests/personal relationships which may be considered as potential competing interests: Xueliang Zhang reports financial support was provided by the National Natural Science Foundation of China.

Data availability

I have explained the publicly available data sources and provided download links in the data section of the article. It is unfortunate that the observation data is not publicly available.

Acknowledgments

This study is jointly supported by the National Natural Science Foundation of China (Grant No. 42171307) and the “GeoX” Interdisciplinary Research Funds for the Frontiers Science Center for Critical Earth Material Cycling, Nanjing University.

References

Anderton, S.P., White, S.M., Alvera, B., 2004. Evaluation of spatial variability in snow water equivalent for a high mountain catchment. Hydrol. Process. 18, 435–453. https://doi.org/10.1002/hyp.1319.

Armstrong, R.L., Brodzik, M.J., 2001. Recent northern hemisphere snow extent: a comparison of data derived from visible and microwave satellite sensors. Geophys. Res. Lett. 28, 3673–3676. https://doi.org/10.1029/2000GL012556.

Baez-Villanueva, O.M., Zambrano-Bigiarini, M., Beck, H.E., McNamara, I., Ribbe, L., Nauditt, A., Birkel, C., Verbist, K., Giraldo-Osorio, J.D., Xuan Thinh, N., 2020. RF-MEP: a novel random Forest method for merging gridded precipitation products and ground-based measurements. Remote Sens. Environ. 239, 111606 https://doi.org/10.1016/j.rse.2019.111606.

Balsamo, G., Albergel, C., Beljaars, A., Boussetta, S., Brun, E., Cloke, H., Dee, D., Dutra, E., Muñoz-Sabater, J., Pappenberger, F., de Rosnay, P., Stockdale, T., Vitart, F., 2015. ERA-interim/land: a global land surface reanalysis data set. Hydrol. Earth Syst. Sci. 19, 389–407. https://doi.org/10.5194/hess-19-389-2015.

Barnett, T.P., Dümenil, L., Schlese, U., Roeckner, E., 1988. The effect of eurasian snow cover on global climate. Science, New Series 239, 504–507.

Barnett, T.P., Adam, J.C., Lettenmaier, D., P,, 2005. Potential impacts of a warming climate on water availability in snow-dominated regions. Nature 438, 303–309. https://doi.org/10.1038/nature04141.

Behrens, T., Schmidt, K., Viscarra Rossel, R.A., Gries, P., Scholten, T., MacMillan, R.A., 2018. Spatial modelling with euclidean distance fields and machine learning: spatial modelling with euclidean distance fields. Eur J Soil Sci 69, 757–770. https://doi.org/10.1111/ejss.12687.

Bentéjac, C., Csörgő, A., Martínez-Muñoz, G., 2021. A comparative analysis of gradient boosting algorithms. Artif Intell Rev 54, 1937–1967. https://doi.org/10.1007/s10462-020-09896-5.

Bian, Q., Xu, Z., Zhao, L., Zhang, Y.-F., Zheng, H., Shi, C., Zhang, S., Xie, C., Yang, Z.-L., 2019. Evaluation and intercomparison of multiple snow water equivalent products over the tibetan plateau. J. Hydrometeorol. 20, 2043–2055. https://doi.org/10.1175/JHM-D-19-0011.1.

Bintanja, R., Andry, O., 2017. Towards a rain-dominated Arctic. Nature Clim Change 7, 263–267. https://doi.org/10.1038/nclimate3240.

Brun, E., Vionnet, V., Boone, A., Decharme, B., Peings, Y., Valette, R., Karbou, F., Morin, S., 2013. Simulation of northern eurasian local snow depth, mass, and density using a detailed snowpack model and meteorological reanalyses. J. Hydrometeorol. 14, 203–219. https://doi.org/10.1175/JHM-D-12-012.1.

Chang, S., Shi, J., Jiang, L., Zhang, L., Yang, H., 2009. Improved snow depth retrieval algorithm in China area using passive microwave remote sensing data, in: 2009 IEEE International Geoscience and Remote Sensing Symposium. Presented at the 2009 IEEE International Geoscience and Remote Sensing Symposium, IEEE, Cape Town, South Africa, p. II-614–II–617. https://doi.org/10.1109/IGARSS.2009.5418161.

Chang, A.T.C., Foster, J.L., Hall, D.K., 1996. EFFECTS of forest on the snow parameters derived from microwave measurements during the boreas WINTER field campaign. Hydrol. Process. 10, 1565–1574. https://doi.org/10.1002/(SICI)1099-1085(199612)10:12<1565::AID-HYP501>3.0.CO;2-5.

Che, T., Dai, L., Zheng, X., Li, X., Zhao, K., 2016. Estimation of snow depth from passive microwave brightness temperature data in forest regions of Northeast China. Remote Sens. Environ. 183, 334–349. https://doi.org/10.1016/j.rse.2016.06.005.

Chen , T. , Guestrin , C. . XGBoost: a scalable tree boosting System. Knowledge Discovry and data Mining . 785 – 794 . https://doi.org/10.1145/2939672.2939785.

Chen, X., Liang, S., Cao, Y., He, T., Wang, D., 2015. Observed contrast changes in snow cover phenology in northern middle and high latitudes from 2001–2014. Sci Rep 5, 16820. https://doi.org/10.1038/srep16820.

Chen, Z.-Y., Zhang, T.-H., Zhang, R., Zhu, Z.-M., Yang, J., Chen, P.-Y., Ou, C.-Q., Guo, Y., 2019. Extreme gradient boosting model to estimate PM2.5 concentrations with missing-filled satellite data in China. Atmos. Environ. 202, 180–189. https://doi.org/10.1016/j.atmosenv.2019.01.027.

China Meteorological Administration (CMA), 2003. Ground meteorological observation specifications. China Meteorological Press, Beijing, China, pp. 151–153 in Chinese.

Dai, L., Che, T., Wang, J., Zhang, P., 2012. Snow depth and snow water equivalent estimation from AMSR-E data based on a priori snow characteristics in Xinjiang, China. Remote Sens. Environ. 127, 14–29. https://doi.org/10.1016/j.rse.2011.08.029.

Dai, L., Che, T., Ding, Y., Hao, X., 2017. Evaluation of snow cover and snow depth on the Qinghai-tibetan plateau derived from passive microwave remote sensing. Cryosphere 11, 1933–1948. https://doi.org/10.5194/tc-11-1933-2017.

Dee, D.P., Uppala, S.M., Simmons, A.J., Berrisford, P., Poli, P., Kobayashi, S., Andrae, U., Balmaseda, M.A., Balsamo, G., Bauer, P., Bechtold, P., Beljaars, A.C.M., van de Berg, L., Bidlot, J., Bormann, N., Delsol, C., Dragani, R., Fuentes, M., Geer, A.J., Haimberger, L., Healy, S.B., Hersbach, H., Hólm, E.V., Isaksen, L., Kållberg, P., Köhler, M., Matricardi, M., McNally, A.P., Monge-Sanz, B.M., Morcrette, J.-J., Park, B.-K., Peubey, C., de Rosnay, P., Tavolato, C., Thépaut, J.-N., Vitart, F., 2011. The ERA-interim reanalysis: configuration and performance of the data assimilation system. Q.J.R. Meteorol. Soc. 137, 553–597. https://doi.org/10.1002/qj.828.

Deems, J.S., Painter, T.H., Finnegan, D.C., 2013. Lidar measurement of snow depth: a review. J. Glaciol. 59, 467–479. https://doi.org/10.3189/2013JoG12J154.

Derksen, C., 2008. The contribution of AMSR-E 18.7 and 10.7 GHz measurements to improved boreal forest snow water equivalent retrievals. Remote Sens. Environ. 112, 2701–2710. https://doi.org/10.1016/j.rse.2008.01.001.

Derksen, C., Walker, A., Goodison, B., 2005. Evaluation of passive microwave snow water equivalent retrievals across the boreal forest/tundra transition of western Canada. Remote Sens. Environ. 96, 315–327. https://doi.org/10.1016/j.rse.2005.02.014.

Dozier, J., Bair, E.H., Davis, R.E., 2016. Estimating the spatial distribution of snow water equivalent in the world's mountains. WIREs Water 3, 461–474. https://doi.org/10.1002/wat2.1140.

Dutra, E., Kotlarski, S., Viterbo, P., Balsamo, G., Miranda, P.M.A., Schär, C., Bissolli, P., Jonas, T., 2011. Snow cover sensitivity to horizontal resolution, parameterizations, and atmospheric forcing in a land surface model: SNOW COVER SENSITIVITY. J. Geophys. Res. 116 https://doi.org/10.1029/2011JD016061.

Essery, R., Pomeroy, J., 2004. Vegetation and topographic control of wind-blown snow distributions in distributed and aggregated simulations for an Arctic Tundra Basin. J. Hydrometeor 5, 735–744. https://doi.org/10.1175/1525-7541(2004)005<0735:VATCOW>2.0.CO;2.

Fan, J., Wang, X., Wu, L., Zhou, H., Zhang, F., Yu, X., Lu, X., Xiang, Y., 2018. Comparison of support vector machine and extreme gradient boosting for predicting daily global solar radiation using temperature and precipitation in humid subtropical climates: a case study in China. Energ. Conver. Manage. 164, 102–111. https://doi.org/10.1016/j.enconman.2018.02.087.

Flanner, M.G., Shell, K.M., Barlage, M., Perovich, D.K., Tschudi, M.A., 2011. Radiative forcing and albedo feedback from the northern hemisphere cryosphere between 1979 and 2008. Nature Geosci 4, 151–155. https://doi.org/10.1038/ngeo1062.

Fontrodona-Bach, A., Schaefli, B., Woods, R., Teuling, A.J., Larsen, J.R., 2023. NH-SWE: northern hemisphere snow water equivalent dataset based on in situ snow depth time series. Earth Syst. Sci. Data 15, 2577–2599. https://doi.org/10.5194/essd-15-2577-2023.

Frei, A., Robinson, D.A., 1999. Northern hemisphere snow extent: regional variability 1972–1994. Int. J. Climatol. 19, 1535–1560. https://doi.org/10.1002/(SICI)1097-0088(19991130)19:14<1535::AID-JOC438>3.0.CO;2-J.

Ganjkhanlo, H., Vafakhah, M., Zeinivand, H., Fathzadeh, A., 2020. The effect of different sampling schemes on estimation precision of snow water equivalent (SWE) using geostatistics techniques in a semi-arid region of Iran. Geocarto Int. 35, 1769–1782. https://doi.org/10.1080/10106049.2019.1581267.

Gelaro, R., McCarty, W., Suárez, M.J., Todling, R., Molod, A., Takacs, L., Randles, C.A., Darmenov, A., Bosilovich, M.G., Reichle, R., Wargan, K., Coy, L., Cullather, R., Draper, C., Akella, S., Buchard, V., Conaty, A., da Silva, A.M., Gu, W., Kim, G.-K., Koster, R., Lucchesi, R., Merkova, D., Nielsen, J.E., Partyka, G., Pawson, S., Putman, W., Rienecker, M., Schubert, S.D., Sienkiewicz, M., Zhao, B., 2017. The modern-era retrospective analysis for research and applications, version 2 (MERRA-2). J. Climate 30, 5419–5454. https://doi.org/10.1175/JCLI-D-16-0758.1.

Griessinger, N., Seibert, J., Magnusson, J., Jonas, T., 2016. Assessing the benefit of snow data assimilation for runoff modeling in Alpine catchments. Hydrol. Earth Syst. Sci. 20, 3895–3905. https://doi.org/10.5194/hess-20-3895-2016.

Hao, X., Huang, G., Che, T., Ji, W., Sun, X., Zhao, Q., Zhao, H., Wang, J., Li, H., Yang, Q., 2021. The NIEER AVHRR snow cover extent product over China – a long-term daily snow record for regional climate research. Earth Syst. Sci. Data 13, 4711–4726. https://doi.org/10.5194/essd-13-4711-2021.

Hengl, T., Nussbaum, M., Wright, M.N., Heuvelink, G.B.M., Gräler, B., 2018. Random Forest as a generic framework for predictive modeling of spatial and spatio-temporal variables (preprint). PeerJ Preprints. https://doi.org/10.7287/peerj.preprints.26693v2.

Hori, M., Sugiura, K., Kobayashi, K., Aoki, T., Tanikawa, T., Kuchiki, K., Niwano, M., Enomoto, H., 2017. A 38-year (1978–2015) northern hemisphere daily snow cover extent product derived using consistent objective criteria from satellite-borne optical sensors. Remote Sens. Environ. 191, 402–418. https://doi.org/10.1016/j.rse.2017.01.023.

Hu, Y., Che, T., Dai, L., Xiao, L., 2021. Snow depth fusion based on machine learning methods for the northern hemisphere. Remote Sens. (Basel) 13, 1250. https://doi.org/10.3390/rs13071250.

Huang, X., Deng, J., Ma, X., Wang, Y., Feng, Q., Hao, X., Liang, T., 2016. Spatiotemporal dynamics of snow cover based on multi-source remote sensing data in China. Cryosphere 10, 2453–2463. https://doi.org/10.5194/tc-10-2453-2016.

Imaoka, K., Kachi, M., Fujii, H., Murakami, H., Hori, M., Ono, A., Igarashi, T., Nakagawa, K., Oki, T., Honda, Y., Shimoda, H., 2010. Global change observation Mission (GCOM) for monitoring carbon, water cycles, and climate change. Proc. IEEE 98, 717–734. https://doi.org/10.1109/JPROC.2009.2036869.

Jiang, L., Wang, P., Zhang, L., Yang, H., Yang, J., 2014. Improvement of snow depth retrieval for FY3B-MWRI in China. Sci. China Earth Sci. 57, 1278–1292. https://doi.org/10.1007/s11430-013-4798-8.

Jiang, L., Yang, J., Zhang, C., Wu, S., Li, Z., Dai, L., Li, X., Qiu, Y., 2022. Daily snow water equivalent product with SMMR, SSM/I and SSMIS from 1980 to 2020 over China. Big Earth Data 1–15. https://doi.org/10.1080/20964471.2022.2032998.

Just, A., De Carli, M., Shtein, A., Dorman, M., Lyapustin, A., Kloog, I., 2018. Correcting measurement error in satellite aerosol optical depth with machine learning for modeling PM2.5 in the northeastern USA. Remote Sens. (Basel) 10, 803. https://doi.org/10.3390/rs10050803.

Karthikeyan, L., Mishra, A.K., 2021. Multi-layer high-resolution soil moisture estimation using machine learning over the United States. Remote Sens. Environ. 266, 112706 https://doi.org/10.1016/j.rse.2021.112706.

Kelly, R., 2009. The AMSR-E snow depth algorithm: description and initial Results[J]. J. Remote Sens. Soc. Jpn. 29 (1), 307–317.

Li, P., Mi, D., 1983. The distribution of snow cover in China. Journal of Glaciology and cryopedology.

Liang, J., Liu, X., Huang, K., Li, X., Shi, X., Chen, Y., Li, J., 2015. Improved snow depth retrieval by integrating microwave brightness temperature and visible/infrared reflectance. Remote Sens. Environ. 156, 500–509. https://doi.org/10.1016/j.rse.2014.10.016.

Luojus, K., Pulliainen, J., Takala, M., Lemmetyinen, J., Mortimer, C., Derksen, C., Mudryk, L., Moisander, M., Hiltunen, M., Smolander, T., Ikonen, J., Cohen, J., Salminen, M., Norberg, J., Veijola, K., Venäläinen, P., 2021. GlobSnow v3.0 northern hemisphere snow water equivalent dataset. Sci Data 8, 163. https://doi.org/10.1038/s41597-021-00939-2.

Ma, Z., Dey, S., Christopher, S., Liu, R., Bi, J., Balyan, P., Liu, Y., 2022. A review of statistical methods used for developing large-scale and long-term PM2.5 models from satellite data. Remote Sens. Environ. 269, 112827 https://doi.org/10.1016/j.rse.2021.112827.

Ma, H., Liang, S., 2022. Development of the GLASS 250-m leaf area index product (version 6) from MODIS data using the bidirectional LSTM deep learning model. Remote Sens. Environ. 273, 112985 https://doi.org/10.1016/j.rse.2022.112985.

Meloche, J., Langlois, A., Rutter, N., McLennan, D., Royer, A., Billecocq, P., Ponomarenko, S., 2022. High-resolution snow depth prediction using random Forest algorithm with topographic parameters: a case study in the greiner watershed. Nunavut. Hydrological Processes 36. https://doi.org/10.1002/hyp.14546.

Molotch, N.P., Margulis, S.A., 2008. Estimating the distribution of snow water equivalent using remotely sensed snow cover data and a spatially distributed snowmelt model: a multi-resolution, multi-sensor comparison. Adv. Water Resour. 31, 1503–1514. https://doi.org/10.1016/j.advwatres.2008.07.017.

Mudryk, L.R., Derksen, C., Kushner, P.J., Brown, R., 2015. Characterization of northern hemisphere snow water equivalent datasets, 1981–2010. J. Climate 28, 8037–8051. https://doi.org/10.1175/JCLI-D-15-0229.1.

Muñoz-Sabater, J., Dutra, E., Agustí-Panareda, A., Albergel, C., Arduini, G., Balsamo, G., Boussetta, S., Choulga, M., Harrigan, S., Hersbach, H., Martens, B., Miralles, D.G., Piles, M., Rodríguez-Fernández, N.J., Zsoter, E., Buontempo, C., Thépaut, J.-N., 2021. ERA5-land: a state-of-the-art global reanalysis dataset for land applications. Earth Syst. Sci. Data 13, 4349–4383. https://doi.org/10.5194/essd-13-4349-2021.

Orsolini, Y., Wegmann, M., Dutra, E., Liu, B., Balsamo, G., Yang, K., De Rosnay, P., Zhu, C., Wang, W., Senan, R., Arduini, G., 2019. Evaluation of snow depth and snow cover over the tibetan plateau in global reanalyses using in situ and satellite remote sensing observations. Cryosphere 13, 2221–2239. https://doi.org/10.5194/tc-13-2221-2019.

Painter, T.H., Berisford, D.F., Boardman, J.W., Bormann, K.J., Deems, J.S., Gehrke, F., Hedrick, A., Joyce, M., Laidlaw, R., Marks, D., Mattmann, C., McGurk, B., Ramirez, P., Richardson, M., Skiles, S.M., Seidel, F.C., Winstral, A., 2016. The airborne snow observatory: fusion of scanning lidar, imaging spectrometer, and physically-based modeling for mapping snow water equivalent and snow albedo. Remote Sens. Environ. 184, 139–152. https://doi.org/10.1016/j.rse.2016.06.018.

Premier, V., Marin, C., Bertoldi, G., Barella, R., Notarnicola, C., Bruzzone, L., 2023. Exploring the use of multi-source high-resolution satellite data for snow water equivalent reconstruction over mountainous catchments. Cryosphere 17, 2387–2407. https://doi.org/10.5194/tc-17-2387-2023.

Pulliainen, J., Luojus, K., Derksen, C., Mudryk, L., Lemmetyinen, J., Salminen, M., Ikonen, J., Takala, M., Cohen, J., Smolander, T., Norberg, J., 2020. Patterns and trends of northern hemisphere snow mass from 1980 to 2018. Nature 581, 294–298. https://doi.org/10.1038/s41586-020-2258-0.

Reichler, T., Kim, J., 2008. Uncertainties in THE climate mean state of global observations, reanalyses, and THE GFDL climate model: UNCERTAINTIES IN THE CLIMATE MEAN. J. Geophys. Res. 113, n/a-n/a. https://doi.org/10.1029/2007JD009278.

Rittger, K., Bair, E.H., Kahl, A., Dozier, J., 2016. Spatial estimates of snow water equivalent from reconstruction. Adv. Water Resour. 94, 345–363. https://doi.org/10.1016/j.advwatres.2016.05.015.

Rodell, M., Houser, P.R., Jambor, U., Gottschalck, J., Mitchell, K., Meng, C.-J., Arsenault, K., Cosgrove, B., Radakovich, J., Bosilovich, M., Entin, J.K., Walker, J.P., Lohmann, D., Toll, D., 2004. The global land data assimilation system. Bull. Amer. Meteor. Soc. 85, 381–394. https://doi.org/10.1175/BAMS-85-3-381.

Rodriguez, J.D., Perez, A., Lozano, J.A., 2010. Sensitivity analysis of k-fold cross validation in prediction error estimation. IEEE Trans. Pattern Anal. Mach. Intell. 32, 569–575. https://doi.org/10.1109/TPAMI.2009.187.

Shao, D., Li, H., Wang, J., Hao, X., Che, T., Ji, W., 2022. Reconstruction of a daily gridded snow water equivalent product for the land region above 45° N based on a ridge regression machine learning approach. Earth Syst. Sci. Data 14, 795–809. https://doi.org/10.5194/essd-14-795-2022.

Snauffer, A.M., Hsieh, W.W., Cannon, A.J., Schnorbus, M.A., 2018. Improving gridded snow water equivalent products in British Columbia, Canada: multi-source data fusion by neural network models. Cryosphere 12, 891–905. https://doi.org/10.5194/tc-12-891-2018.

Sturm, M., Wagner, A.M., 2010. Using repeated patterns in snow distribution modeling: an Arctic example: REPEATED SNOW PATTERNS. Water Resour. Res. 46 https://doi.org/10.1029/2010WR009434.

Sun, Y., Zhang, T., Liu, Y., Zhao, W., Huang, X., 2020. Assessing snow phenology over the large part of Eurasia using satellite observations from 2000 to 2016. Remote Sens. (Basel) 12, 2060. https://doi.org/10.3390/rs12122060.

Takala, M., Luojus, K., Pulliainen, J., Derksen, C., Lemmetyinen, J., Kärnä, J.-P., Koskinen, J., Bojkov, B., 2011. Estimating northern hemisphere snow water equivalent for climate research through assimilation of space-borne radiometer data and ground-based measurements. Remote Sens. Environ. 115, 3517–3529. https://doi.org/10.1016/j.rse.2011.08.014.

Tedesco, M., Jeyaratnam, J., 2019. AMSR-E/AMSR2 unified L3 global daily 25 km EASE-grid snow water E quivalent, version 1. NASA National Snow and Ice Data Center Distributed Active Archive Center, Boulder, Colorado USA [online].

Trujillo, E., Ramírez, J.A., Elder, K.J., 2007. Topographic, meteorologic, and canopy controls on the scaling characteristics of the spatial distribution of snow depth fields: SPATIAL SCALING OF SNOW DEPTH. Water Resour. Res. 43 https://doi.org/10.1029/2006WR005317.

Vafakhah, M., Nasiri Khiavi, A., Janizadeh, S., Ganjkhanlo, H., 2022. Evaluating different machine learning algorithms for snow water equivalent prediction. Earth Sci Inform 15, 2431–2445. https://doi.org/10.1007/s12145-022-00846-z.

Wang, H., Zhang, X., Xiao, P., Zhang, K., Wu, S., 2022. Elevation-dependent response of snow phenology to climate change from a remote sensing perspective: a case survey in the central tianshan mountains from 2000 to 2019. Intl Journal of Climatology 42, 1706–1722. https://doi.org/10.1002/joc.7330.

Wei, J., Li, Z., Lyapustin, A., Sun, L., Peng, Y., Xue, W., Su, T., Cribb, M., 2021. Reconstructing 1-km-resolution high-quality PM2.5 data records from 2000 to 2018 in China: spatiotemporal variations and policy implications. Remote Sens. Environ. 252, 112136 https://doi.org/10.1016/j.rse.2020.112136.

Wei, J., Liu, S., Li, Z., Liu, C., Qin, K., Liu, X., Pinker, R.T., Dickerson, R.R., Lin, J., Boersma, K.F., Sun, L., Li, R., Xue, W., Cui, Y., Zhang, C., Wang, J., 2022. Ground-level NO_2 surveillance from space across China for high resolution using interpretable spatiotemporally weighted artificial intelligence. Environ. Sci. Technol. 56, 9988–9998. https://doi.org/10.1021/acs.est.2c03834.

Xu, X., Liu, J., Zhang, S., Li, R., Yan, C., Wu, S., 2018. China multi-period land use land cover remote sensing monitoring data set (CNLUCC). Chinese Academy of Sciences, Resources and Environment Science Data Center https://doi.org/10.12078/2018070201.

Yang, J., Jiang, L., Ménard, C.B., Luojus, K., Lemmetyinen, J., Pulliainen, J., 2015. Evaluation of snow products OVER THE tibetan plateau: EVALUATION OF SNOW PRODUCTS OVER THE TIBETAN PLATEAU. Hydrol. Process. 29, 3247–3260. https://doi.org/10.1002/hyp.10427.

Yang, J., Jiang, L., Wu, S., Wang, G., Wang, J., Liu, X., 2019. Development of a snow depth estimation algorithm over China for the FY-3D/MWRI. Remote Sens. (Basel) 11, 977. https://doi.org/10.3390/rs11080977.

Yang, J., Jiang, L., Lemmetyinen, J., Luojus, K., Takala, M., Wu, S., Pan, J., 2020a. Validation of remotely sensed estimates of snow water equivalent using multiple reference datasets from the middle and high latitudes of China. J. Hydrol. 590, 125499 https://doi.org/10.1016/j.jhydrol.2020.125499.

Yang, J., Jiang, L., Luojus, K., Pan, J., Lemmetyinen, J., Takala, M., Wu, S., 2020b. Snow depth estimation and historical data reconstruction over China based on a random forest machine learning approach. Cryosphere 14, 1763–1778. https://doi.org/10.5194/tc-14-1763-2020.

Yang, N., Shi, H., Tang, H., Yang, X., 2022. Geographical and temporal encoding for improving the estimation of PM2.5 concentrations in China using end-to-end gradient boosting. Remote Sens. Environ. 269, 112828 https://doi.org/10.1016/j.rse.2021.112828.

Friedman, J., 2001. Greedy function approximation: a gradient boosting machine. The Annals of Statistics. 29, 1189–1232. doi: http://www.jstor.org/stable/2699986.